



Article

Interface Engineering of CoFe-LDH Modified Ti: α -Fe₂O₃ Photoanode for Enhanced Photoelectrochemical Water Oxidation

Yue Chang^{1,2,3,*} , Minmin Han^{4,5}, Yehui Ding¹, Huiyun Wei⁶, Dawei Zhang^{1,2,3}, Hong Luo^{1,2}, Xiaogang Li^{1,2} and Xiongbo Yan⁷

¹ Institute of Advanced Materials and Technology, University of Science and Technology Beijing, Beijing 100083, China

² National Materials Corrosion and Protection Data Center, University of Science and Technology Beijing, Beijing 100083, China

³ BRI Southeast Asia Network for Corrosion and Protection (MOE), Shunde Innovation School, University of Science and Technology Beijing, Foshan 528399, China

⁴ National Engineering Research Center for Intelligent Electrical Vehicle Power System, College of Mechanical and Electrical Engineering, Qingdao University, Qingdao 266071, China

⁵ International Center for Materials Nanoarchitectonics (WPI-MANA), National Institute for Materials Science (NIMS), 1-1 Namiki, Tsukuba 305-0044, Ibaraki, Japan

⁶ School of Mathematics and Physics, University of Science and Technology Beijing, Beijing 100083, China

⁷ Beijing Advanced Innovation Center Materials Genome Engineering, University of Science and Technology Beijing, Beijing 100083, China

* Correspondence: changyue@ustb.edu.cn

Abstract: Effectively regulating and promoting the charge separation and transfer of photoanodes is a key and challenging aspect of photoelectrochemical (PEC) water oxidation. Herein, a Ti-doped hematite photoanode with a CoFe-LDH cocatalyst loaded on the surface was prepared through a series of processes, including hydrothermal treatment, annealing and electrodeposition. The prepared CoFe-LDH/Ti: α -Fe₂O₃ photoanode exhibited an outstanding photocurrent density of 3.06 mA/cm² at 1.23 V_{RHE}, which is five times higher than that of α -Fe₂O₃ alone. CoFe-LDH modification and Ti doping on hematite can boost the surface charge transfer efficiency, which is mainly attributed to the interface interaction between CoFe-LDH and Ti: α -Fe₂O₃. Furthermore, we investigated the role of Ti doping in enhancing the PEC performance of CoFe-LDH/Ti: α -Fe₂O₃. A series of characterizations and theoretical calculations revealed that, in addition to improving the electronic conductivity of the bulk material, Ti doping also further enhances the interface coupling of CoFe-LDH/ α -Fe₂O₃ and finely regulates the interfacial electronic structure. These changes promote the rapid extraction of holes from hematite and facilitate charge separation and transfer. The informative findings presented in this work provide valuable insights for the design and construction of hematite photoanodes, offering guidance for achieving excellent performance in photoelectrochemical (PEC) water oxidation.

Keywords: CoFe-LDH; titanium doping; hematite; interface coupling enhancement; photoelectrochemical water oxidation



Citation: Chang, Y.; Han, M.; Ding, Y.; Wei, H.; Zhang, D.; Luo, H.; Li, X.; Yan, X. Interface Engineering of CoFe-LDH Modified Ti: α -Fe₂O₃ Photoanode for Enhanced Photoelectrochemical Water Oxidation. *Nanomaterials* **2023**, *13*, 2579. <https://doi.org/10.3390/nano13182579>

Academic Editor: Hong Seok Kang

Received: 12 August 2023

Revised: 14 September 2023

Accepted: 15 September 2023

Published: 18 September 2023



Copyright: © 2023 by the authors. Licensee MDPI, Basel, Switzerland. This article is an open access article distributed under the terms and conditions of the Creative Commons Attribution (CC BY) license (<https://creativecommons.org/licenses/by/4.0/>).

1. Introduction

Photoelectrochemical (PEC) water splitting has attracted considerable attention owing to the urgent requirement for sustainable and clean hydrogen energy. This technology holds the potential to effectively tackle the economic and environmental challenges associated with fossil fuels [1,2]. The process of PEC water splitting, which separates water into hydrogen and oxygen, involves a complex multi-electron reaction, driven by the generation of electron-hole pairs within a semiconductor catalyst under light irradiation. In PEC water splitting, the oxygen evolution reaction (OER) requires four electrons to complete, making it more challenging than the two-electrons hydrogen evolution reaction (HER) [3,4]. In

this case, the development of efficient photoanode materials has become one of pivotal problems for PEC water splitting. Among various photoanode materials, hematite stands out due to its narrow band gap (~2.1 eV), its high theoretical solar-to-hydrogen efficiency (15.3%), its abundance in the Earth's crust and its good chemical stability [5,6]. However, the PEC performance of hematite can be limited, which is attributed to the high rate of recombination of photoinduced electron-hole pairs, and the low efficiency of hole injection. The limitations result in practical efficiencies far below the theoretical values [7,8].

The surface modification of hematite with oxygen evolution cocatalysts (OECs) has been demonstrated as an effective approach to address the issues mentioned above [9–11]. Layered double hydroxides (LDHs), which contain edge-sharing octahedral MO_6 units, are ideal candidates due to their unique layered structure and compositional versatility. Previous work has reported on introduced LDHs, such as NiFe-LDHs [12], NiCe-LDHs [13], ZnCo-LDHs [14] and CoAl-LDHs [15], onto hematite photoanodes to enhance PEC performance. Among the LDHs, CoFe-LDHs have attracted research interest for (photo)electrocatalytic water oxidation due to the synergistic effect of Fe and Co, which can enhance OER activity [16–18]. Xu et al. [19] reported on engineering interfaces to steer hole dynamics in BiVO_4 photoanodes for solar water oxidation. CoFe-LDHs were decorated on the surface of a $\text{BiVO}_4/\text{Co}_3\text{O}_4$ photoanode using cathodic electrodeposition, demonstrating further enhancement in PEC performance. However, an undesirable interface between the semiconductor and LDHs cocatalyst can have a detrimental effect on PEC water oxidation.

Elemental doping combined with surface modification represents one of the most effective strategies for addressing the low activity of hematite in PEC water oxidation [20,21]. Metal ion dopants, such as Ti^{4+} acting as donor impurities, have been widely reported for their role in enhanced PEC performance of hematite photoanodes [22,23]. Ti^{4+} doping can improve the electronic conductivity of hematite by regulating its electronic structure. For surface modified photoanodes, such as OEC decorated hematite, the regulated electronic structure and increased carrier density of hematite inevitably result in the change in interface states between the OECs and hematite [24,25]. Consequently, during PEC water oxidation, the charge separation and transfer on the surface and interface are affected. Therefore, it is expected that Ti doping may improve surface or interface charge transfer and enhance favorable interactions at the interface, rather than just solely focusing on changes in bulk conductivity resulting from donor doping.

Inspired by the above discussion, we successfully fabricated a CoFe-LDH/Ti: α - Fe_2O_3 photoanode via the hydrothermal treatment–annealing–electrodeposition method. Ti doping played an important role for the CoFe-LDH/ α - Fe_2O_3 photoanode for enhancing the PEC performance of water oxidation. We found that Ti doping not only improves the charge separation of bulk hematite, but also enhances the surface charge transfer and charge injection into the electrolyte by enhancing the interface coupling effect and regulating the interfacial electronic structure between CoFe-LDH and α - Fe_2O_3 . This work contributes to a deeper understanding of the mechanisms behind the enhancement of photoanodes for photoelectrochemical (PEC) water oxidation, providing new insights on improving surface and interface charge separation and transfer.

2. Experimental Details

2.1. Synthesis of Photoanodes

According to previous reports [22,26], the hematite materials with or without Ti doping were prepared on the conductive surface of fluorine-doped tin oxide substrates ($14 \Omega/\text{cm}^2$, Wuhan Lattice Solar Technology, Wuhan, China) via a hydrothermal–annealing method. More specifically, firstly, the precursor solution was prepared through dissolving 0.15 M $\text{FeCl}_3 \cdot 6\text{H}_2\text{O}$ (AR, Aladdin, Shanghai, China) and 1 M NaNO_3 (AR, Sinopharm Chemical Reagent, Shanghai, China). For Ti-doped hematite materials, 0.11 M titanium tetrachloride (AR, Aladdin, Shanghai, China) in ethanol solution with a volume of 16 μL was added to the precursor solution, in which the Ti/Fe content ratio in feed was consistent with 0.3 wt%. After that, five pieces of cleaned fluorine-doped tin oxide glass were placed

into a Teflon-lined autoclave, in which the fluorine-doped tin oxide conductive was face down against the wall of the autoclave. The prepared precursor solution was added into the autoclave and immersed the fluorine-doped tin oxide glass. This autoclave was then heated to 100 °C for 4 h. The obtained yellow materials attached to the surface of the fluorine-doped tin oxide glass were β -FeOOH or Ti-doped β -FeOOH. Finally, the obtained samples were washed with deionized water, and annealed in air at 550 °C for 2 h in a muffle furnace and at 700 °C for 20 min in a muffle furnace. The as-prepared Ti-doped α -Fe₂O₃ films were designated as TFO.

According to previous reports [19,27], CoFe-LDH materials were prepared on the surface of the hematite substrates, with or without Ti doping, through a simple electrodeposition method. In a typical procedure, we prepare a mixture of 0.006 M Co(NO₃)₂ (AR, Energy Chemical, Shanghai, China) and 0.006 M Fe(NO₃)₃ (AR, Aladdin, Shanghai, China) in aqueous solutions as the electrodeposited electrolyte. A three-electrode configuration was used, where the substrate served as the working electrode, a platinum plate as the counter electrode, and an Ag/AgCl electrode as the reference electrode. The electrodeposition of CoFe-LDH was conducted under a constant voltage of $-0.8 V_{Ag/AgCl}$ with a deposition time of 80 s. Subsequently, the working electrodes were thoroughly washed with copious amounts of water. The obtained samples with different substrates were designated as CoFe-LDH/ α -Fe₂O₃ and CoFe-LDH/TFO, respectively.

2.2. Characterization

The morphology was observed through a ZEISS GeminiSEM 300 field emission scanning electron microscope (FE-SEM, ZEISS, Oberkochen, Germany) and an FEI Tecnai G2 F20 transmission electron microscope (TEM, FEI, Oberkochen, Germany). The X-ray diffraction (XRD) patterns for all the samples were analyzed using a Rigaku SmartLab X-ray diffractometer (Cu K α radiation, Rigaku, Tokyo, Japan) with a scan range of 2 θ from 10 to 80° and a scan rate of 6°/min. The diffuse UV-Vis absorption spectra were recorded using a Shimadzu spectrophotometer (UV-2700, Shimadzu, Kyoto, Japan) equipped with an integral sphere in the range of 300–800 nm. The XPS spectra of the samples were measured by a PHI Quantera II spectrometer (ULVAC-PHI, Kanagawa, Japan), using Al K α X-ray as the excitation source. All the spectra were calibrated using the C1s binding energy at 284.8 eV as the reference.

2.3. Photoelectrochemical Measurements

The photoelectrochemical (PEC) experiments were performed on a CHI660E electrochemical workstation in a typical three-electrode configuration with a 1 M NaOH aqueous solution serving as the electrolyte. The prepared photoanodes were employed as the working electrode. A platinum plate (1 × 1 cm²) and a Ag/AgCl electrode were employed as the counter electrode and the reference electrode, respectively. The exposed area of the photoanode immersed in the aqueous electrolyte was controlled to be 0.2826 cm². A 300 W Xe lamp equipped with an AM 1.5 filter was used to simulate solar light irradiation, and the light intensity was adjusted to 100 mW/cm². All the measured potentials (vs. Ag/AgCl) were converted to the RHE scale using the following Equation (1):

$$E_{RHE} = E_{Ag/AgCl} + 0.059pH + E_{Ag/AgCl}^0 \quad (1)$$

where E_{RHE} and $E_{Ag/AgCl}$ refer to the converted potential vs. the RHE and the measured potential vs. Ag/AgCl, respectively. $E_{Ag/AgCl}^0 = 0.197 V$ at 25 °C. The photocurrent-potential curves were generated through linear sweep voltammetry (LSV) measurements within a voltage range of 0.5 V to 1.5 V vs. the RHE at a scanning rate of 10 mV/s. The transient photocurrent densities were recorded in cycles of 20 s at a potential of 1.23 V vs. the RHE. The applied bias photon-to-current efficiency (ABPE) was calculated using the following Equation (2):

$$ABPE(\%) = \frac{J \times (1.23 - V_b)}{P_{total}} \quad (2)$$

where J represents the photocurrent density (mA/cm^2), V_b is the applied bias vs. the RHE, and P_{total} refers to the total light intensity of AM 1.5 G ($100 \text{ mW}/\text{cm}^2$). The IPCE measurements for all the photoanodes were conducted using a monochromator (Omno151, NBET, Beijing, China). The IPCE spectra were measured at 1.23 V vs. the RHE, with 10 nm steps in the wavelength range of 350 nm~600 nm. The incident photon-to-current conversion efficiency (IPCE) is calculated using the following Equation (3):

$$IPCE = \frac{1240 \times I}{\lambda \times P_{light}} \quad (3)$$

where λ represents the wavelength of the incident light, and I and P_{light} are the measured photocurrent density and irradiance at some specific wavelengths. The water oxidation photocurrent density can be calculated using the following Equation (4):

$$J_{PEC} = J_{abs} \times \eta_{sep} \times \eta_{inj} \quad (4)$$

where J_{abs} represents the photocurrent density from the photon completely absorbed into the current. As a hole scavenger, Na_2SO_3 can effectively trap the holes that arrive at the surface, and there is no influence on the charge separation on the electrode (η_{inj} assumed to be 100%). Therefore, the charge separation efficiency of the bulk (η_{sep}) and the charge transfer efficiency of the surface (η_{inj}) can be given by the following Equations (5) and (6):

$$\eta_{sep} = \frac{J_{\text{Na}_2\text{SO}_3}}{J_{abs}} \quad (5)$$

$$\eta_{trans} = \frac{J_{\text{H}_2\text{O}}}{J_{\text{Na}_2\text{SO}_3}} \quad (6)$$

where $J_{\text{H}_2\text{O}}$ and $J_{\text{Na}_2\text{SO}_3}$ represent the photocurrent densities measured in 1 M NaOH electrolyte without and with 1 M Na_2SO_3 , respectively. The EIS measurements were conducted with 1.23 V_{RHE} potential over the frequency range of 0.05 Hz to 1 MHz under simulated solar irradiation. Mott-Schottky data were collected in the dark at a scan rate of 50 mV/s with a frequency of 1 kHz in the potential range from -0.5 to 0.5 V vs. Ag/AgCl.

3. Results and Discussion

3.1. C and Characterization of the As-Synthesized Photoanode Materials

The fabrication process of the CoFe-LDH/Ti: α - Fe_2O_3 film is illustrated in Figure 1a. Firstly, yellow Ti-doped β -FeOOH nanorods were grown on a conductive glass substrate using the hydrothermal method and, subsequently, transformed into red Ti-doped α - Fe_2O_3 (TFO) through annealing. Finally, the CoFe-LDH was decorated on the surface of the TFO via a common cathodic electrodeposition method for LDH materials [19,27]. Figure 1 and Figure S1 (Supplementary Materials) display the SEM and TEM images of the α - Fe_2O_3 , TFO and CoFe-LDH/TFO samples. The vertically aligned nanorods of α - Fe_2O_3 can be observed in Figure 1b–d, with the average diameters ranging from 70 to 100 nm and a thickness of approximately 500 to 600 nm (Figure S1a). This indicates that the nanorod-like structure is still well preserved (Figure 1c), although the surface of the CoFe-LDH/TFO appears slightly rough (Figure 1d). The TEM and HRTEM images in Figure 1e,f further confirm the nanosheet morphology of CoFe-LDH with a thickness of 2 to 10 nm. Additionally, the HRTEM image clearly reveals a lattice spacing of 0.274 nm, corresponding well to the (104) plane of α - Fe_2O_3 . In another region, no lattice fringes are visible, indicating the amorphous state of CoFe-LDH. The EDS elemental mapping images for a selected region are shown in Figure S1b. These results demonstrated the even distribution of the Fe, O, Ti and Co elements, indicating the successful doping of the Ti element and decoration of the CoFe-LDH nanosheets on hematite.

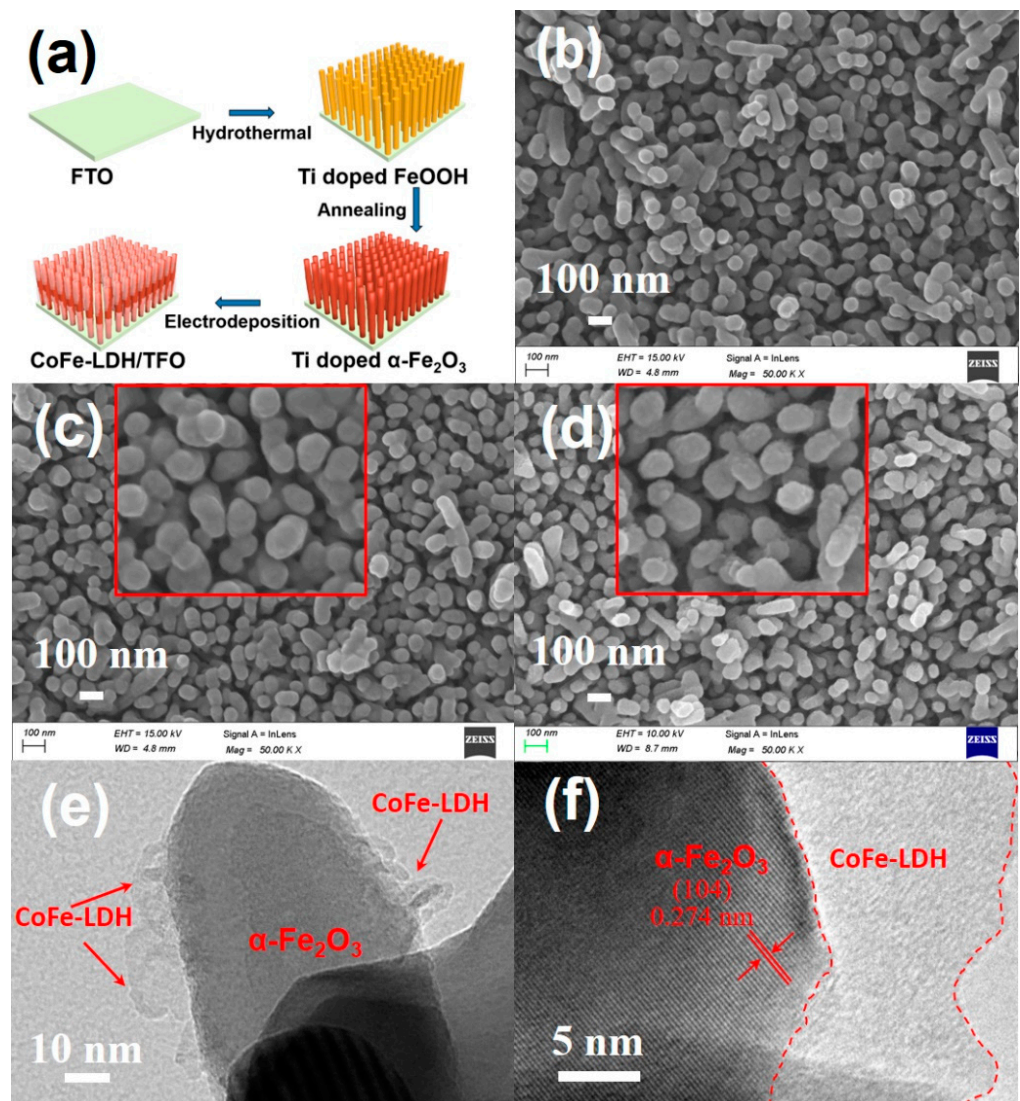


Figure 1. (a) The synthesis procedure of CoFe-LDH/Ti:α-Fe₂O₃ photoanode; SEM images of (b) α-Fe₂O₃, (c) TFO and (d) CoFe-LDH/TFO; (e) TEM image and (f) HRTEM image of CoFe-LDH/TFO.

The XRD patterns of the α-Fe₂O₃, TFO and CoFe-LDH/TFO films in Figure S1c exhibit similar characteristic peaks. These diffraction peaks can all be indexed to α-Fe₂O₃ (JCPDS No. 86-0550) and SnO₂ derived from the fluorine-doped tin oxide substrate (JCPDS No. 41-1445). There are no obvious changes in the diffraction peaks after Ti doping and CoFe-LDH deposition. This is due to the low concentration of Ti dopants and the amorphous structure of CoFe-LDH, which is consistent with the HRTEM results. The DRS UV-Vis spectra of the α-Fe₂O₃, TFO, CoFe-LDH/α-Fe₂O₃ and CoFe-LDH/TFO photoanodes are presented in Figure S1d. The absorption edge of α-Fe₂O₃ is located at approximately 583 nm. It can be observed that the introduction of CoFe-LDH does not significantly alter the absorption spectra of CoFe-LDH/α-Fe₂O₃ and CoFe-LDH/TFO compared with α-Fe₂O₃ and TFO, respectively. This indicates the good optical transparency of CoFe-LDH. However, Ti doping leads to a slight redshift in the absorption edges for the TFO and CoFe-LDH/TFO samples compared with α-Fe₂O₃ and CoFe-LDH/α-Fe₂O₃, respectively. The band gap energies of the above samples were calculated based on the $(\alpha h\nu)^2 - h\nu$ curves [28] (Figure S2b (inset)). The E_g values of α-Fe₂O₃ and CoFe-LDH/α-Fe₂O₃ are approximately 2.08 eV, while those of TFO and CoFe-LDH/TFO are around 2.13 eV. This suggests that the Ti elements were successfully doped into the bulk of α-Fe₂O₃, resulting in a slight enhancement of the visible light absorption.

To further confirm the electrodeposition of CoFe-LDH on the surface of the TFO, the XPS analysis of the CoFe-LDH/TFO samples was conducted to determine the surface elemental composition and chemical state. The high-resolution XPS spectra of Fe 2p, O1s, Co 2p and Ti 2p are presented in Figure 2a–d. As shown in Figure 2a, in the Fe 2p XPS spectrum, the binding energies of 711.0 eV and 724.5 eV correspond to the peaks of Fe 2p_{3/2} and Fe 2p_{1/2}, respectively. Followed by fitting deconvolution, the two peaks at 713.3 eV and 727.2 eV are assigned to the Fe³⁺ in CoFe-LDH, the two peaks of lower binding energy centered at 711.1 eV and 724.3 eV represent the Fe³⁺ in α -Fe₂O₃, and the other two peaks at 709.7 eV and 722.4 eV are assigned to the Fe²⁺ of α -Fe₂O₃ [29,30]. Additionally, the observable Fe³⁺ satellite peaks at 718.7 eV and 733.8 eV are consistent with the presence of Fe³⁺ in α -Fe₂O₃ and CoFe-LDH [31,32]. The O1s peaks of the CoFe-LDH/TFO samples can be deconvoluted into three peaks, as seen in Figure 2b. The binding energies centered at 529.8 eV, 531.3 eV and 532.2 eV can be assigned to the lattice oxygen species in hematite, the hydroxyl groups of CoFe-LDH and the absorbed H₂O, respectively [33]. In Figure 2c, the Co 2p XPS spectrum shows two major peaks at binding energies of Co 2p_{3/2} and Co 2p_{1/2}, accompanying two satellite peaks located at 787.5 eV and 803.1 eV. After further fitting of the Co 2p_{3/2} and Co 2p_{1/2}, the binding energies at 781.0 eV and 797.2 eV can be attributed to the Co²⁺ in CoFe-LDH [34]. Moreover, the Ti 2p XPS spectrum of the CoFe-LDH/TFO samples is presented in Figure 2d. The peaks at 458.2 eV and 464.1 eV correspond to the Ti⁴⁺ 2p_{3/2} and Ti⁴⁺ 2p_{1/2} peaks, respectively, indicating the presence of Ti⁴⁺ in the TFO [23]. The observation of the Ti 2p XPS spectra confirms the successful doping of Ti, which is consistent with the results of the DRS UV–Vis analysis.

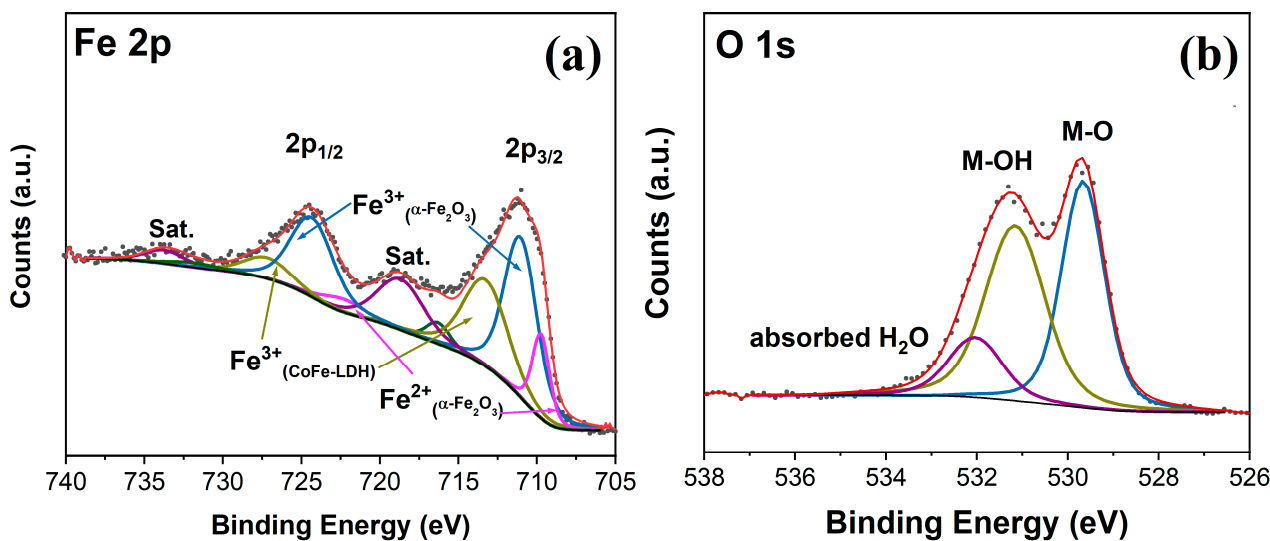


Figure 2. Cont.

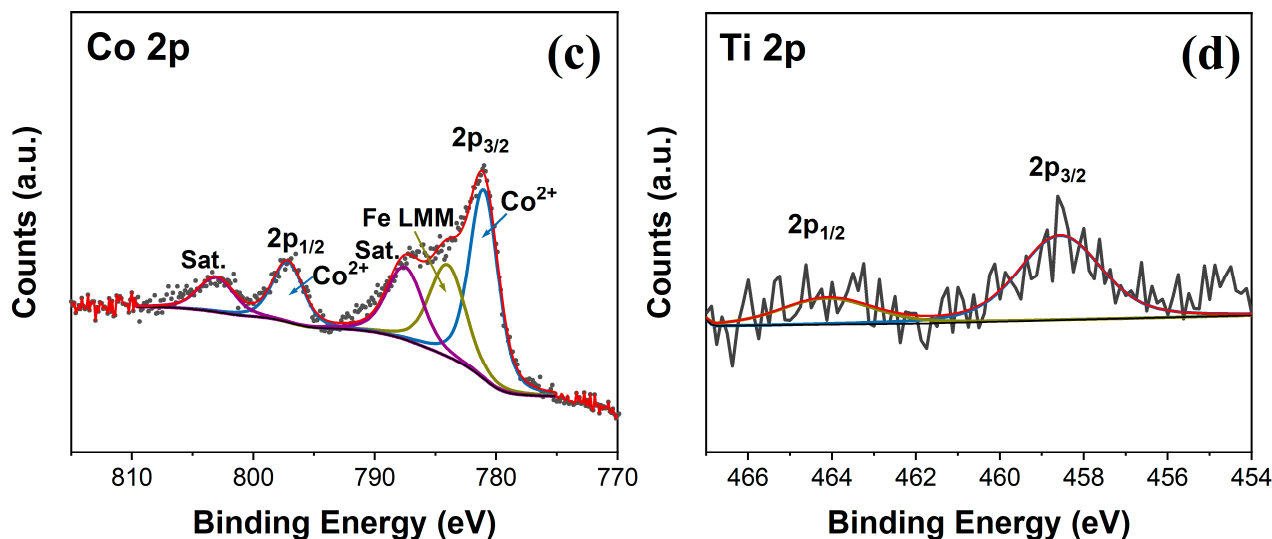


Figure 2. High-resolution XPS spectra of (a) Fe 2p; (b) O 1s; (c) Co 2p and (d) Ti 2p in the CoFe-LDH/TFO samples.

3.2. The PEC Performance of Water Oxidation for Photoanodes

The PEC performance of the as-prepared α -Fe₂O₃, TFO, CoFe-LDH/ α -Fe₂O₃ and CoFe-LDH/TFO photoanodes was investigated through LSV curves under light irradiation. As exhibited in Figure 3a, the α -Fe₂O₃ photoanode presents a low photocurrent density of 0.62 mA/cm² at 1.23 V_{RHE}. The TFO photoanode, on the other hand, displays a higher photocurrent density (1.37 mA/cm² at 1.23 V_{RHE}), attributed to the Ti dopant increasing the donor density and enhancing the electrical conductivity of the α -Fe₂O₃ film [22,23]. By further electrodepositing CoFe-LDH on the surface of α -Fe₂O₃ and TFO, the photocurrent densities are both increased, reaching 3.06 mA/cm² at 1.23 V_{RHE}. Notably, the current of CoFe-LDH/TFO in the dark is negligible, indicating that the improvement in the photocurrent arises from the photoelectric conversion process. An apparent cathodic shift in the onset potential is observed for CoFe-LDH/TFO and CoFe-LDH/ α -Fe₂O₃, shifting from 0.81 V_{RHE} of α -Fe₂O₃ and 0.80 V_{RHE} of TFO to 0.72 V_{RHE} of CoFe-LDH/ α -Fe₂O₃ and 0.74 V_{RHE} of CoFe-LDH/TFO, respectively. Moreover, the steady-state photocurrents were determined by the I-t curve at 1.23 V_{RHE} (Figure 3b and Figure S2), and the results are in good agreement with the LSV results. The photocurrent density of the CoFe-LDH/TFO photoanodes remains constant over 3600 s of light irradiation. Figure 3c illustrates the applied bias photo-to-current efficiency (ABPE) values of all the photoanodes calculated from the LSV curves. The ABPE values of CoFe-LDH/TFO reach up to 0.41% at 1.00 V_{RHE}, significantly exceeding those of TFO (0.14% at 1.03 V_{RHE}), α -Fe₂O₃ (0.09% at 1.01 V_{RHE}) and CoFe-LDH/ α -Fe₂O₃ (0.23% at 0.97 V_{RHE}). The incident photon-to-current conversion efficiency (IPCE) was also obtained in the wavelength range of 350–600 nm. According to Figure 3d, the CoFe-LDH/TFO photoanodes exhibit the highest IPCE values (34.2% at 350 nm), which are four times higher than those of α -Fe₂O₃ (7.6% at 350 nm). These results indicate that the enhancement of the PEC performance in CoFe-LDH/TFO can be mainly attributed to the synergistic effects of the Ti dopant and CoFe-LDH nanosheets.

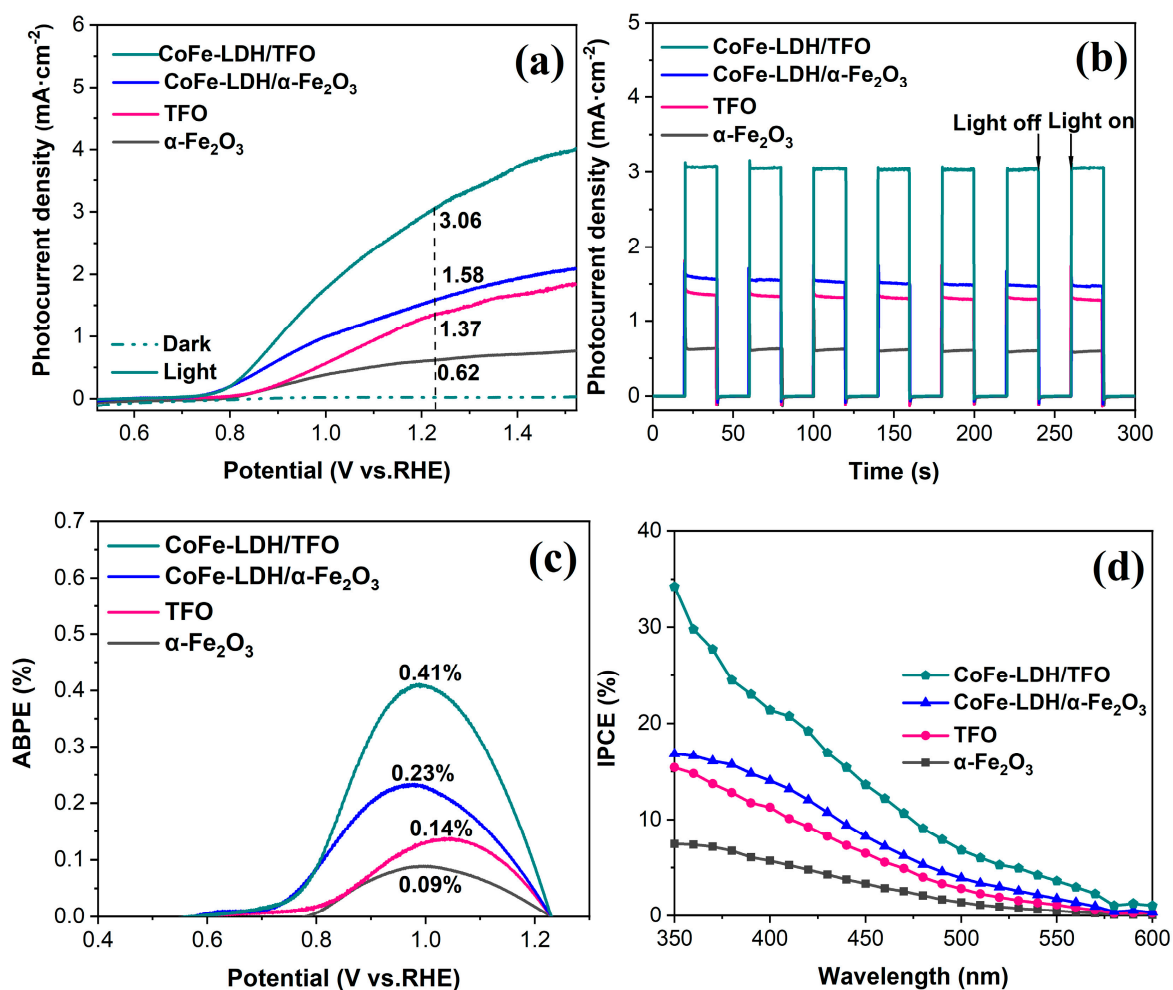


Figure 3. (a) LSV curves, (b) photocurrent-time curves at 1.23 V_{RHE}, (c) ABPE curves and (d) IPCE curves at 1.23 V_{RHE} of α -Fe₂O₃, TFO, CoFe-LDH/ α -Fe₂O₃ and CoFe-LDH/TFO photoanodes.

3.3. The Effect of Ti Dopants and CoFe-LDH Deposition on the Charge Transfer Process of the Photoanodes

To understand the catalytic effect of Ti doping and CoFe-LDH deposition, we investigated the charge transfer and separation behaviors through a series of electrochemical measurements. Mott–Schottky plots were used to determine the carrier densities (N_d) and flat-band potentials of the α -Fe₂O₃, TFO, CoFe-LDH/ α -Fe₂O₃ and CoFe-LDH/TFO samples. Figure 4a shows a linear relationship of $(1/C)^2$ vs. the potential. Compared with α -Fe₂O₃, all the other photoanodes show distinctly smaller slopes, with the smallest observed for CoFe-LDH/TFO. The carrier densities were calculated based on the Mott–Schottky slopes, and the results are listed in Table S1. However, it should be noted that these data were primarily suitable for comparison due to the accurate capacitance calculation based on the grounds of the flat structure [35,36]. Among the four photoanodes, CoFe-LDH/TFO exhibits the highest carrier density. The introduction of Ti as dopants obviously increases the carrier densities of hematite, promoting the separation of photogenerated electron–hole pairs. Additionally, CoFe-LDH, as cocatalysts, enhances the carrier densities of hematite, contributing to band bending at the electrode–electrolyte interface and accelerating interfacial charge transfer [37–39].

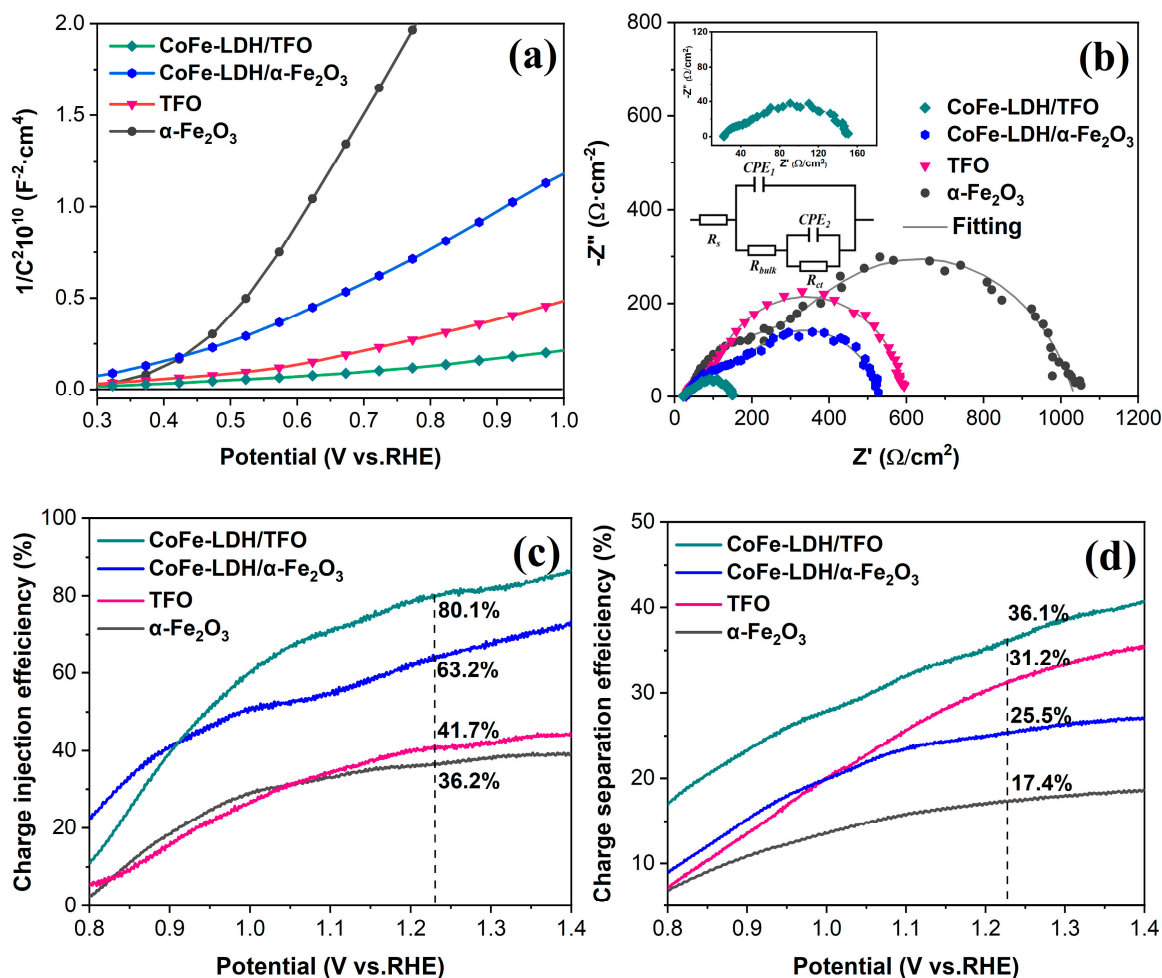


Figure 4. (a) Mott–Schottky plots, (b) EIS at $1.23 V_{RHE}$ under light irradiation (R_s , R_{bulk} , R_{ct} and CPE refer to the series resistance, the charge trapping resistance in bulk with high frequency, the charge transfer resistance across the interface of the photoanode and electrolyte with low frequency and the constant phase element, respectively), (c) the charge injection efficiency and (d) charge separation efficiency of $\alpha\text{-Fe}_2\text{O}_3$, TFO, CoFe-LDH/ $\alpha\text{-Fe}_2\text{O}_3$ and CoFe-LDH/TFO photoanodes.

To gain insights into the impact of Ti doping and CoFe-LDH deposition on the charge transfer process, the EIS measurements were conducted at a potential of $1.23 V_{RHE}$ under light irradiation (Figure 4b). An equivalent circuit was employed to fit the EIS data (see inset of Figure 4b), and the fitting values are listed in Table 1. The Nyquist plots for the four photoanodes show two semicircles, representing the charge trapping resistance within the bulk and the charge transfer resistance at the interface between the photoanode and the electrolyte. An enlarged impedance view of CoFe-LDH/TFO is shown in the inset of Figure 4b. Ti doping reduces the R_{bulk} from 391.9Ω to 93.7Ω , indicating that Ti dopants reduce the charge trapping resistance in the bulk [40]. CoFe-LDH plays a crucial role in hole transport into the electrolyte, evident from the significantly lower R_{ct} value of CoFe-LDH/ $\alpha\text{-Fe}_2\text{O}_3$ (283.7Ω) compared to $\alpha\text{-Fe}_2\text{O}_3$ (613.3Ω) and TFO (475.6Ω). Compared to the other three photoanodes, the synergistic effects of Ti doping and CoFe-LDH cocatalysts result in a remarkable decrease in the R_{bulk} and R_{ct} values of CoFe-LDH/TFO [36]. Notably, the ratios of the R_{bulk} and R_{ct} of Ti-doped CoFe-LDH/ $\alpha\text{-Fe}_2\text{O}_3$ to $\alpha\text{-Fe}_2\text{O}_3$ are higher than those of non-Ti-doped CoFe-LDH/ $\alpha\text{-Fe}_2\text{O}_3$ to $\alpha\text{-Fe}_2\text{O}_3$, suggesting that Ti doping enhances the electronic conductivity of $\alpha\text{-Fe}_2\text{O}_3$ and may promote the surface charge transfer effect of the CoFe-LDH cocatalysts on the photoanodes.

Table 1. The equivalent circuit model EIS results for different photoanodes.

Photoanodes	R_s (Ω)	R_{bulk} (Ω)	R_{ct} (Ω)
α -Fe ₂ O ₃	30.5	391.9	613.3
TFO	29.8	93.7	475.6
CoFe-LDH/ α -Fe ₂ O ₃	27.5	228.8	283.7
CoFe-LDH/TFO	22.5	32.4	96.6

In order to further confirm the improved charge transfer and separation of CoFe-LDH/TFO, the role of Ti doping in the interfacial charge separation and transfer process was investigated. The LSV measurements used 1 M Na₂SO₃ as a hole scavenger under light irradiation. The rapid hole injection kinetics during the oxidation of Na₂SO₃ allow for the complete capture of the separated holes [3,41], the charge separation efficiencies in the bulk (η_{sep}) and the charge injection efficiencies on the surface (η_{inj}) can be calculated using Equations (4)–(6), and the related plots are provided in Figure S3. As shown in Figure 4c,d, the η_{sep} values for the TFO and CoFe-LDH/TFO photoanodes at 1.23 V_{RHE} are 31.2% and 36.1%, respectively, which are significantly higher than the values of 17.4% for α -Fe₂O₃ and 25.5% for CoFe-LDH/ α -Fe₂O₃. This suggests that Ti doping enhances the electron–hole separation in hematite, and the introduction of CoFe-LDH further improves this separation through hole extraction [42]. Regarding the charge injection on the surface, there is a substantial increase in the η_{inj} after CoFe-LDH deposition, from 36.2% to 63.2% at 1.23 V_{RHE}. This increases CoFe-LDH’s ability to promote hole injection into the electrolyte for water oxidation. The η_{inj} of TFO also shows a slight increase compared to that of α -Fe₂O₃ at 1.23 V_{RHE}. Notably, the difference in the charge injection efficiencies between CoFe-LDH/TFO and TFO is higher than that between CoFe-LDH/ α -Fe₂O₃ and α -Fe₂O₃. This suggests that Ti doping significantly enhances the charge injection in CoFe-LDH/ α -Fe₂O₃ compared with α -Fe₂O₃. In other words, Ti doping enhances the cocatalytic ability of CoFe-LDH for hematite photoanodes, consistent with the results from the EIS.

3.4. The Promoting Mechanism of CoFe-LDH/TFO Photoanodes for Water Oxidation

It has been discussed and proven that surface modification with CoFe-LDH enhances the charge separation and transfer efficiencies of TFO. The remarkably enhanced photocurrent density observed after CoFe-LDH deposition can be attributed to several factors. Firstly, the good optical transparency (Figure S1d) of CoFe-LDH reduces light absorption losses in the photoanodes, facilitating the formation of more photogenerated holes and electrons [19,43]. Additionally, we found the presence of an interfacial coupling between CoFe-LDH and α -Fe₂O₃. In order to study the effect of Ti doping on the CoFe-LDH/ α -Fe₂O₃ photoanodes, we prepared CoFe-LDH/TFO with a double amount of Ti doping (denoted as CoFe-LDH/TDFO) using the same synthesis method as for CoFe-LDH/TFO (the Ti 2p XPS spectra of CoFe-LDH/TFO and CoFe-LDH/TDFO are exhibited in Figure 5a). The high-resolution Co 2p and Fe 2p XPS spectra of CoFe-LDH/ α -Fe₂O₃ and CoFe-LDH/TDFO were investigated, as shown in Figure 5b,c, and the corresponding peak fitting results were similar to those of CoFe-LDH/TFO [29,30,34]. However, in the XPS spectra of Co 2p_{3/2} in Figure 5b, we observed noticeable negative shifts of 0.13 eV for CoFe-LDH/TFO and 0.28 eV for CoFe-LDH/TDFO compared to CoFe-LDH/ α -Fe₂O₃. With increased Ti doping, these negative shifts became more pronounced. Furthermore, in Figure 5c, we observed that the Fe 2p_{3/2} peaks of α -Fe₂O₃ shifted towards higher binding energy with increasing Ti doping, while the Fe 2p_{3/2} peaks of CoFe-LDH shifted towards lower binding energy. These observations indicate the presence of the interface coupling effect between CoFe-LDH and α -Fe₂O₃ with Ti doping [44]. Notably, stronger coupling was observed with increased Ti doping, resulting in a partial electron transfer from α -Fe₂O₃ to CoFe-LDH, which explains the observed shifts [45].

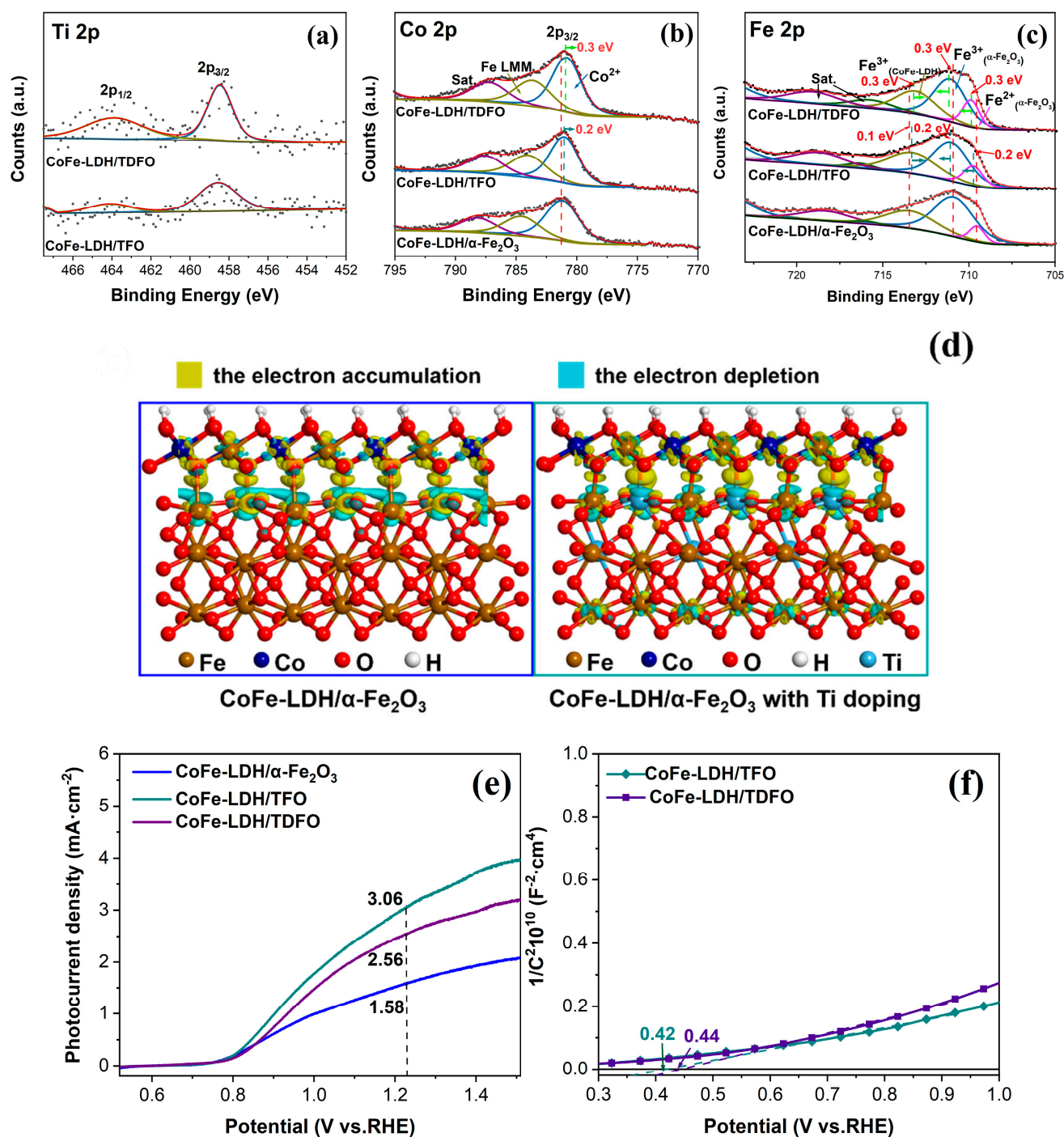


Figure 5. High-resolution XPS spectra of (a) Ti 2p of CoFe-LDH/TFO and CoFe-LDH/TDFO samples; (b) Co 2p and (c) Fe 2p of CoFe-LDH/ α -Fe₂O₃, CoFe-LDH/TFO and CoFe-LDH/TDFO samples; (d) the charge density difference between the optimized structures of CoFe-LDH/ α -Fe₂O₃ and CoFe-LDH/ α -Fe₂O₃ with Ti doping; (e) LSV curves of CoFe-LDH/ α -Fe₂O₃, CoFe-LDH/TFO and CoFe-LDH/TFO photoanodes; (f) Mott–Schottky plots for CoFe-LDH/TFO and CoFe-LDH/TFO photoanodes.

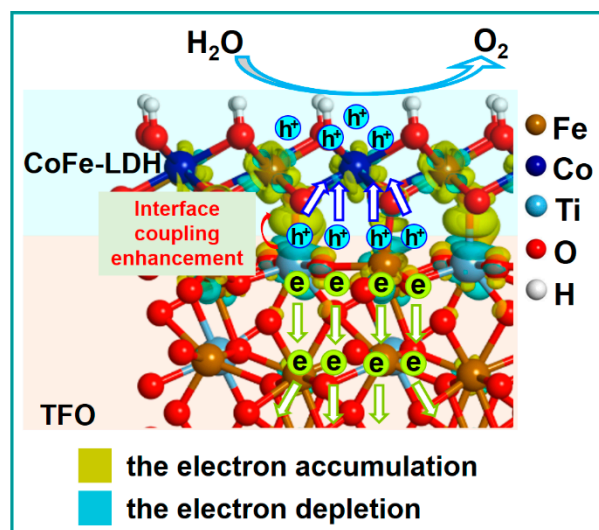
The first-principles calculations were carried out to gain insights into the electron interactions between CoFe-LDH and α -Fe₂O₃. The optimized structures of CoFe-LDH/ α -Fe₂O₃ with and without Ti doping are shown in Figure S4. To further investigate the effects of Ti doping, we examined the charge density differences over CoFe-LDH/ α -Fe₂O₃

and CoFe-LDH/ α -Fe₂O₃, as illustrated in Figure 5d. In both cases, we observed electron depletion regions (depicted in blue) and the electron accumulation regions (depicted in yellow). Notably, the yellow regions (electron accumulation) were mainly located on CoFe-LDH, while the blue regions (electron depletion) were mainly located on α -Fe₂O₃. This suggests that there is an electron transfer occurring between CoFe-LDH and α -Fe₂O₃, both with and without Ti doping [46].

Furthermore, the changes in charge density for CoFe-LDH and α -Fe₂O₃ can be observed in Figure 5d. After Ti doping, the number of electrons transferred between CoFe-LDH and α -Fe₂O₃ increased from 0.969 to 1.024, based on quantitative Bader charge analysis. This indicates a stronger electron transfer between CoFe-LDH and α -Fe₂O₃ after Ti doping. These results are consistent with the conclusions drawn from the XPS analysis (Figure 5b,c). In addition, the results are supported by the quantitative analysis of the calculated average Bader charge (Table S2). The valences of Co and Fe in Ti-doped CoFe-LDH decreased from 1.269 to 1.195 and from 1.503 to 1.378, respectively, indicating an increase in the number of valence electrons for Co and Fe. This is caused by the stronger electron shielding effect caused by Ti doping and aligns with the XPS results mentioned above [47].

Based on the results of the XPS analysis and the theoretical calculations, it was found that CoFe-LDH has interface coupling interactions with α -Fe₂O₃, which are further enhanced by Ti doping. The electron accumulation in CoFe-LDH facilitates the extraction of photo-induced holes and repels electrons. The stronger electron accumulation induced by Ti doping accelerates the charge transfer, allowing CoFe-LDH to accept holes more easily [46,48]. This explains the higher surface charge injection efficiency observed after Ti doping. However, despite the strongest electron coupling interaction between CoFe-LDH and α -Fe₂O₃ in CoFe-LDH/TDFO, it exhibited only a moderate photocurrent density (Figure 5e). The reason for the lower photocurrent density in CoFe-LDH/TDFO compared with CoFe-LDH/TFO can be attributed to the positive shift in the flat-band potential and the decrease in the carrier density, according to the Mott–Schottky plots in Figure 5f. These results indicate that Ti doping finely regulates the electronic structure at the interface between CoFe-LDH and α -Fe₂O₃, enhancing the interfacial charge separation and transfer. Consequently, this enhancement leads to the superior PEC performance of CoFe-LDH/TFO for water oxidation.

Based on the preceding discussions, we have illustrated the charge transfer pathways for CoFe-LDH/TFO photoanodes in Scheme 1 to clarify the enhancement of the photoelectrochemical water oxidation performance. Under light irradiation, α -Fe₂O₃ is excited, generating photoinduced electron–hole pairs. When Ti is doped into hematite, the increased electronic conductivity in the bulk enables the photogenerated electrons and holes to migrate more rapidly to the fluorine-doped tin oxide substrate and the surface. Subsequently, CoFe-LDH is deposited onto the hematite surface. Thanks to the enhanced electron accumulation within CoFe-LDH, which is a result of Ti doping, the photogenerated holes can be extracted more efficiently to CoFe-LDH, limiting carrier recombination [8,47]. Co ions can act as active sites for receiving holes from α -Fe₂O₃. These received holes are then oxidized to high-valent states [49]. Because of the presence of electron accumulation, Co sites become more receptive to accepting holes. This increased receptivity facilitates Co ions in delivering a positive charge, which, in return, promotes the formation of reactant OOH intermediates, thus accelerating O₂ evolution [8,48].



Scheme 1. The charge transfer paths supposed to be occurring in CoFe-LDH/TiO₂ photoanode for PEC water oxidation.

4. Conclusions

In summary, we have demonstrated the important role of Ti-doped hematite photoanodes with CoFe-LDH deposited on the surface, which were successfully synthesized and applied to PEC water oxidation. The resulting CoFe-LDH/TiO₂ photoanode exhibited an outstanding photocurrent density of 3.06 mA/cm² at 1.23 V_{RHE}, which is five times higher than that of pristine hematite. The charge separation of the bulk and the injection efficiencies of the surface were increased up to 36.1% and 80.1%, respectively, compared with those of hematite (17.4% and 36.2%). The enhancement of the PEC performance can be ascribed to the interface interaction between CoFe-LDH and Ti:α-Fe₂O₃. Ti doping plays a dual role: it improves the electronic conductivity of hematite and enhances the interface coupling effect, as well as regulating the interfacial electron structure between CoFe-LDH and α-Fe₂O₃. These combined effects effectively accelerate both the bulk and surface charge transfer processes.

Supplementary Materials: The following supporting information can be downloaded at: <https://www.mdpi.com/article/10.3390/nano13182579/s1>, Figure S1: (a) The cross-sectional SEM image of α-Fe₂O₃, (b) EDS elemental mapping in a selected region of CoFe-LDH/TiO₂, (c) XRD spectra of TiO₂, CoFe-LDH/TiO₂ and CoFe-LDH/TiO₂ films on the fluorine-doped tin oxide glass, (d) DR UV-Vis spectra of α-Fe₂O₃, TiO₂, CoFe-LDH/α-Fe₂O₃ and CoFe-LDH/TiO₂. Figure S2: The photocurrent stability test for CoFe-LDH/TiO₂ photoanode. Figure S3: (a) The LSV curves of α-Fe₂O₃, TiO₂, CoFe-LDH/α-Fe₂O₃ and CoFe-LDH/TiO₂ photoanodes with Na₂SO₃ as the hole scavenger; (b) the light harvesting efficiency (LHE) curves of α-Fe₂O₃, TiO₂, CoFe-LDH/α-Fe₂O₃ and CoFe-LDH/TiO₂ samples; (c) the energy density flux of AM 1.5 G solar; and (d) the calculated current density flux of (a) α-Fe₂O₃, (b) TiO₂, (c) CoFe-LDH/α-Fe₂O₃ and (d) CoFe-LDH/TiO₂. Figure S4: The optimized structures of CoFe-LDH/α-Fe₂O₃ and CoFe-LDH/α-Fe₂O₃ with Ti doping. Table S1: The calculated results on the carrier density and flat-band potential of α-Fe₂O₃, TiO₂, CoFe-LDH/α-Fe₂O₃ and CoFe-LDH/TiO₂ from the Mott-Schottky measurements. Table S2: The calculated average Bader charge of the Co atom and Fe atom. Refs. [8,35,50–54] are cited in the Supplementary Materials.

Author Contributions: Formal analysis, Y.C. and M.H.; Investigation, Y.C., Y.D. and H.W.; Resources, M.H., Y.D. and H.W.; Data curation, Y.C. and X.Y.; Writing—original draft, Y.C.; Writing—review & editing, D.Z., H.L. and X.L.; Funding acquisition, Y.C. and H.W. All authors have read and agreed to the published version of the manuscript.

Funding: This work was supported by the fund of the Guangdong Basic and Applied Basic Research Foundation (2021A1515110741) and fund of the Fundamental Research Funds for the Central Universities (Grant No. FRF-IDRY-GD22-001 and Grant No. FRF-GF-19-031B).

Data Availability Statement: Not applicable.

Conflicts of Interest: The authors declare no conflict of interest.

References

1. Ta, X.M.C.; Daiyan, R.; Nguyen, T.K.A.; Amal, R.; Thanh, T.P.; Tricoli, A. Alternatives to Water Photooxidation for Photoelectrochemical Solar Energy Conversion and Green H₂ Production. *Adv. Energy Mater.* **2022**, *12*, 202201358. [[CrossRef](#)]
2. Gondolini, A.; Sangiorgi, N. A Sangiorgi and A Sanson. Photoelectrochemical Hydrogen Production by Screen-Printed Copper Oxide Electrodes. *Energies* **2021**, *14*, 2942. [[CrossRef](#)]
3. Yi, S.S.; Wang, Z.Y.; Li, H.M.; Zafar, Z.; Zhang, Z.T.; Zhang, L.Y.; Chen, D.L.; Liu, Z.Y.; Yue, X.Z. Coupling effects of indium oxide layer on hematite enabling efficient photoelectrochemical water splitting. *Appl. Catal. B Environ.* **2021**, *283*, 119649. [[CrossRef](#)]
4. Yang, W.; Prabhakar, R.R.; Tan, J.; Tilley, S.D.; Moon, J. Strategies for enhancing the photocurrent, photovoltage, and stability of photoelectrodes for photoelectrochemical water splitting. *Chem. Soc. Rev.* **2019**, *48*, 4979–5015. [[CrossRef](#)]
5. Zhang, H.; Li, P.; Zhou, H.; Xu, J.; Jiang, Q.; Hadden, J.H.L.; Wang, Y.; Wang, M.; Chen, S.; Xie, F.; et al. Unravelling the synergy of oxygen vacancies and gold nanostars in hematite for the electrochemical and photoelectrochemical oxygen evolution reaction. *Nano Energy* **2022**, *94*, 106968. [[CrossRef](#)]
6. Yoon, K.Y.; Park, J.; Lee, H.; Seo, J.H.; Kwak, M.; Lee, J.H.; Jang, J. Unveiling the Role of the Ti Dopant and Viable Si Doping of Hematite for Practically Efficient Solar Water Splitting. *ACS Catal.* **2022**, *12*, 5112–5122. [[CrossRef](#)]
7. Ahart, C.S.; Rosso, K.M.; Blumberger, J. Electron and Hole Mobilities in Bulk Hematite from Spin-Constrained Density Functional Theory. *J. Am. Chem. Soc.* **2022**, *144*, 4623–4632. [[CrossRef](#)]
8. Yang, G.L.; Li, Y.X.; Pang, H.; Chang, K.; Ye, J.H. Ultrathin Cobalt–Manganese Nanosheets: An Efficient Platform for Enhanced Photoelectrochemical Water Oxidation with Electron-Donating Effect. *Adv. Funct. Mater.* **2019**, *29*, 1904622. [[CrossRef](#)]
9. Bedin, K.C.; Muche, D.N.F.; Melo, M.A.; Freitas, A.L.M.; Goncalves, R.V.; Souza, F.L. Role of Cocatalysts on Hematite Photoanodes in Photoelectrocatalytic Water Splitting: Challenges and Future Perspectives. *ChemCatChem* **2020**, *12*, 3156–3169. [[CrossRef](#)]
10. Wang, P.P.; Fu, P.; Ma, J.P.; Gao, Y.Y.; Li, Z.; Wang, H.; Fan, F.T.; Shi, J.Y.; Li, C. Ultrathin Cobalt Oxide Interlayer Facilitated Hole Storage for Sustained Water Oxidation over Compositated Tantalum Nitride Photoanodes. *ACS Catal.* **2021**, *11*, 12736–12744. [[CrossRef](#)]
11. Ning, X.M.; Du, P.Y.; Han, Z.G.; Chen, J.; Lu, X.Q. Insight into the Transition-Metal Hydroxide Cover Layer for Enhancing Photoelectrochemical Water Oxidation. *Angew. Chem. Int. Ed.* **2021**, *60*, 3504–3509. [[CrossRef](#)] [[PubMed](#)]
12. Wang, Y.; Liu, L.; Zhang, J.; Zhang, W.; Yao, W.; Jiang, G. NiFe-layered Double Hydroxide/Vertical Bi₂WO₆ Nanoplate Arrays with Oriented {001} Facets Supported on ITO Glass: Improved Photoelectrocatalytic Activity and Mechanism Insight. *ChemCatChem* **2021**, *13*, 3414–3420. [[CrossRef](#)]
13. Sun, C.; Liu, J.; Li, L.; Cheng, J.; Peng, Y.; Xie, Q. Photoanode synthesis of ammonia based on a light reflex strategy and NiCe-layered double hydroxide and oxygen-vacancy Bi₂O₃ catalysts. *Chem. Eng. J.* **2023**, *464*, 142447. [[CrossRef](#)]
14. Wang, H.; Xia, Y.; Wang, X.; Han, Y.; Jiao, X.; Chen, D. Interfacial Coupling Effect on Electron Transport in Hierarchical TaON/Au/ZnCo-LDH Photoanode with Enhanced Photoelectrochemical Water Oxidation. *ACS Appl. Mater. Inter.* **2019**, *11*, 33062–33073. [[CrossRef](#)]
15. Zhong, Y.; Wu, C.; Jia, X.; Sun, S.; Chen, D.; Yao, W.; Ding, H.; Zhang, J.; Ma, T. Coupling of self-healing atomic layer CoAl-LDH onto Mo:BiVO₄ photoanode for fast surface charge transfer toward stable and high-performance water splitting. *Chem. Eng. J.* **2023**, *465*, 142893. [[CrossRef](#)]
16. Chung, D.Y.; Lopes, P.P.; Martins, P.F.B.D.; He, H.; Kawaguchi, T.; Zapol, P.; You, H.; Tripkovic, D.; Strmcnik, D.; Zhu, Y.; et al. Dynamic stability of active sites in hydr(oxy)oxides for the oxygen evolution reaction. *Nat. Energy* **2020**, *5*, 222–230. [[CrossRef](#)]
17. Hung, S.F.; Chan, Y.T.; Chang, C.C.; Tsai, M.K.; Liao, Y.F.; Hiraoka, N.; Hsu, C.S.; Chen, H.M. Identification of Stabilizing High-Valent Active Sites by Operando High-Energy Resolution Fluorescence-Detected X-ray Absorption Spectroscopy for High-Efficiency Water Oxidation. *J. Am. Chem. Soc.* **2018**, *140*, 17263–17270. [[CrossRef](#)]
18. Bhowmik, T.; Kundu, M.K.; Barman, S. CoFe Layered Double Hydroxide Supported on Graphitic Carbon Nitrides: An Efficient and Durable Bifunctional Electrocatalyst for Oxygen Evolution and Hydrogen Evolution Reactions. *Acs Appl. Energy Mater.* **2018**, *1*, 1200–1209. [[CrossRef](#)]
19. Xu, X.; Jin, S.; Yang, C.; Pan, J.; Du, W.; Hu, J.; Zeng, H.; Zhou, Y. Engineering Interfaces to Steer Hole Dynamics of BiVO₄ Photoanodes for Solar Water Oxidation. *Sol. RRL* **2019**, *3*, 1900115. [[CrossRef](#)]
20. Dhandole, L.K.; Anushkaran, P.; Chae, W.-S.; Chung, H.S.; Lee, H.H.; Choi, S.H.; Cho, M.; Jang, J.S. Efficient charge transfers in hematite photoanode integrated by fluorine and zirconia co-doping for photoelectrochemical water splitting. *Chem. Eng. J.* **2022**, *446*, 136957. [[CrossRef](#)]
21. Chen, S.; Huang, D.L.; Xu, P.A.; Xue, W.J.; Lei, L.; Cheng, M.; Wang, R.Z.; Liu, X.G.; Deng, R. Semiconductor-based photocatalysts for photocatalytic and photoelectrochemical water splitting: Will we stop with photocorrosion? *J. Mater. Chem. A* **2020**, *8*, 2286–2322. [[CrossRef](#)]
22. Liu, G.; Zhao, Y.; Yao, R.; Li, N.; Wang, M.; Ren, H.; Li, J.; Zhao, C. Realizing high performance solar water oxidation for Ti-doped hematite nanoarrays by synergistic decoration with ultrathin cobalt-iron phosphate nanolayers. *Chem. Eng. J.* **2019**, *355*, 49–57. [[CrossRef](#)]

23. Apriandanu, D.O.B.; Nomura, S.; Nakayama, S.; Tateishi, C.; Amano, F. Effect of two-step annealing on photoelectrochemical properties of hydrothermally prepared Ti-doped Fe₂O₃ films. *Catal. Today* **2023**, *411–412*, 113826. [[CrossRef](#)]
24. Bai, J.; Gao, R.-T.; Guo, X.; He, J.; Liu, X.; Zhang, X.; Wang, L. Reduction of charge carrier recombination by Ce gradient doping and surface polarization for solar water splitting. *Chem. Eng. J.* **2022**, *448*, 137602. [[CrossRef](#)]
25. Quang, N.D.; Van, P.C.; Majumder, S.; Jeong, J.-R.; Kim, D.; Kim, C. Rational construction of S-doped FeOOH onto Fe₂O₃ nanorods for enhanced water oxidation. *J. Colloid Interf. Sci.* **2022**, *616*, 749–758. [[CrossRef](#)] [[PubMed](#)]
26. Fu, Z.; Jiang, T.; Liu, Z.; Wang, D.; Wang, L.; Xie, T. Highly photoactive Ti-doped α -Fe₂O₃ nanorod arrays photoanode prepared by a hydrothermal method for photoelectrochemical water splitting. *Electrochim. Acta.* **2014**, *129*, 358–363. [[CrossRef](#)]
27. Zhu, Y.K.; Zhao, X.L.; Li, J.Z.; Zhang, H.W.; Chen, S.; Han, W.; Yang, D.J. Surface modification of hematite photoanode by NiFe layered double hydroxide for boosting photoelectrocatalytic water oxidation. *J. Alloy. Compd.* **2018**, *764*, 341–346. [[CrossRef](#)]
28. Chang, Y.; Xuan, Y.; Zhang, C.; Hao, H.; Yu, K.; Liu, S. Z-Scheme Pt@CdS/3DOM-SrTiO₃ composite with enhanced photocatalytic hydrogen evolution from water splitting. *Catal. Today* **2019**, *327*, 315–322. [[CrossRef](#)]
29. Ding, P.; Luo, F.; Wang, P.; Xia, W.; Xu, X.; Hu, J.; Zeng, H. Photo-induced charge kinetic acceleration in ultrathin layered double hydroxide nanosheets boosts the oxygen evolution reaction. *J. Mater. Chem. A* **2020**, *8*, 1105–1112. [[CrossRef](#)]
30. Yi, S.S.; Wulan, B.R.; Yan, J.-M.; Jiang, Q. Highly Efficient Photoelectrochemical Water Splitting: Surface Modification of Cobalt-Phosphate-Loaded Co₃O₄/Fe₂O₃ p-n Heterojunction Nanorod Arrays. *Adv. Funct. Mater.* **2019**, *29*, 1801902. [[CrossRef](#)]
31. Bai, S.; Chu, H.; Xiang, X.; Luo, R.; He, J.; Chen, A. Fabricating of Fe₂O₃/BiVO₄ heterojunction based photoanode modified with NiFe-LDH nanosheets for efficient solar water splitting. *Chem. Eng. J.* **2018**, *350*, 148–156. [[CrossRef](#)]
32. Wang, G.; Ling, Y.; Wheeler, D.A.; George, K.E.N.; Horsley, K.; Heske, C.; Zhang, J.Z.; Li, Y. Facile Synthesis of Highly Photoactive α -Fe₂O₃-Based Films for Water Oxidation. *Nano Lett.* **2011**, *11*, 3503–3509. [[CrossRef](#)] [[PubMed](#)]
33. Gao, L.; Wang, P.; Chai, H.; Li, S.; Jin, J.; Ma, J. Expediting hole transfer via surface states in hematite-based composite photoanodes. *Nanoscale* **2022**, *14*, 17044–17052. [[CrossRef](#)] [[PubMed](#)]
34. Lv, J.; Liu, P.; Li, R.; Wang, L.; Zhang, K.; Zhou, P.; Huang, X.; Wang, G. Constructing accelerated charge transfer channels along V-Co-Fe via introduction of V into CoFe-layered double hydroxides for overall water splitting. *Appl. Catal. B Environ.* **2021**, *298*, 120587. [[CrossRef](#)]
35. Zhang, K.; Dong, T.; Xie, G.; Guan, L.; Guo, B.; Xiang, Q.; Dai, Y.; Tian, L.; Batool, A.; Jan, S.U.; et al. Sacrificial Interlayer for Promoting Charge Transport in Hematite Photoanode. *ACS Appl. Mater. Inter.* **2017**, *9*, 42723–42733. [[CrossRef](#)] [[PubMed](#)]
36. Wang, C.; Long, X.; Wei, S.; Wang, T.; Li, F.; Gao, L.; Hu, Y.; Li, S.; Jin, J. Conformally Coupling CoAl-Layered Double Hydroxides on Fluorine-Doped Hematite: Surface and Bulk Co-Modification for Enhanced Photoelectrochemical Water Oxidation. *ACS Appl. Mater. Inter.* **2019**, *11*, 29799–29806. [[CrossRef](#)]
37. Laskowski, F.A.L.; Nellist, M.R.; Qiu, J.; Boettcher, S.W. Metal Oxide/(oxy)hydroxide Overlayers as Hole Collectors and Oxygen-Evolution Catalysts on Water-Splitting Photoanodes. *J. Am. Chem. Soc.* **2019**, *141*, 1394–1405. [[CrossRef](#)]
38. Liu, W.; Liu, H.; Dang, L.; Zhang, H.; Wu, X.; Yang, B.; Li, Z.; Zhang, X.; Lei, L.; Jin, S. Amorphous Cobalt-Iron Hydroxide Nanosheet Electrocatalyst for Efficient Electrochemical and Photo-Electrochemical Oxygen Evolution. *Adv. Funct. Mater.* **2017**, *27*, 1603904. [[CrossRef](#)]
39. Bergamini, L.; Sangiorgi, N. A Gondolini and A Sanson. Hematite heterostructures for photoelectrochemical water splitting: Rational materials design and charge carrier dynamics. *Solar Energy* **2020**, *212*, 62–72. [[CrossRef](#)]
40. Yu, Z.; Chen, L.; Luo, L.; Huang, R.; Tang, Z.; Xiao, P.; Zhang, Y. Combining Bulk Charge Transport and Surface Charge Transfer to Design Titanium-Doped Hematite Homostructure Photoanodes. *J. Phys. Chem. C* **2022**, *126*, 4296–4305. [[CrossRef](#)]
41. Miao, Y.; Li, Z.; Song, Y.; Fan, K.; Guo, J.; Li, R.; Shao, M. Surface active oxygen engineering of photoanodes to boost photoelectrochemical water and alcohol oxidation coupled with hydrogen production. *Appl. Catal. B Environ.* **2023**, *323*, 122147. [[CrossRef](#)]
42. Bu, Q.; Zhao, Q.; Sun, G.; Liu, Q.; Xie, T. Boosting the photogenerated hole separation and injection of Ti-Fe₂O₃ by co-modifying carbon quantum dots and NiFe layered double hydroxide. *J. Alloy Compd.* **2022**, *908*, 164643. [[CrossRef](#)]
43. Zhang, B.; Wang, L.; Zhang, Y.; Ding, Y.; Bi, Y. Ultrathin FeOOH Nanolayers with Abundant Oxygen Vacancies on BiVO₄ Photoanodes for Efficient Water Oxidation. *Angew. Chem. Int. Ed.* **2018**, *57*, 2248–2252. [[CrossRef](#)]
44. Wang, C.; Sun, S.; Zhang, H.; Zhang, J.; Li, C.; Chen, W.; Li, S. Regulating the Charge Migration in CuInSe₂/N-Doped Carbon Nanorod Arrays via Interfacial Engineering for Boosting Photoelectrochemical Water Splitting. *Adv. Sci.* **2023**, *4*, 2300034. [[CrossRef](#)]
45. Li, T.; Feng, C.; Yap, B.K.; Zhu, X.; Xiong, B.; He, Z.; Wong, W.Y. Accelerating charge transfer via nonconjugated polyelectrolyte interlayers toward efficient versatile photoredox catalysis. *Commun. Chem.* **2021**, *4*, 150. [[CrossRef](#)]
46. Hu, L.; Zeng, X.; Wei, X.; Wang, H.; Wu, Y.; Gu, W.; Shi, L.; Zhu, C. Interface engineering for enhancing electrocatalytic oxygen evolution of NiFe LDH/NiTe heterostructures. *Appl. Catal. B Environ.* **2020**, *273*, 119014. [[CrossRef](#)]
47. Zhao, S.; Jin, R.; Abroshan, H.; Zeng, C.; Zhang, H.; House, S.D.; Gottlieb, E.; Kim, H.J.; Yang, J.C.; Jin, R. Gold Nanoclusters Promote Electrocatalytic Water Oxidation at the Nanocluster/CoSe₂ Interface. *J. Am. Chem. Soc.* **2017**, *139*, 1077–1080. [[CrossRef](#)]
48. Tang, T.; Jiang, W.J.; Niu, S.; Liu, N.; Luo, H.; Chen, Y.Y.; Jin, S.F.; Gao, F.; Wan, L.J.; Hu, J.S. Electronic and Morphological Dual Modulation of Cobalt Carbonate Hydroxides by Mn Doping toward Highly Efficient and Stable Bifunctional Electrocatalysts for Overall Water Splitting. *J. Am. Chem. Soc.* **2017**, *139*, 8320–8328. [[CrossRef](#)]

49. Tang, R.; Zhou, S.; Zhang, Z.; Zheng, R.; Huang, J. Engineering Nanostructure-Interface of Photoanode Materials Toward Photoelectrochemical Water Oxidation. *Adv. Mater.* **2021**, *3*, 2005389. [[CrossRef](#)]
50. Kresse, G.; Furthmüller, J. Efficiency of Ab-Initio Total Energy Calculations for Metals and Semiconductors Using a Plane-Wave Basis Set. *Comput. Mater. Sci.* **1996**, *6*, 15–50. [[CrossRef](#)]
51. Perdew, J.P.; Burke, K.; Ernzerhof, M. Generalized gradient approximation made simple. *Phys. Rev. Lett.* **1996**, *77*, 3865–3868. [[CrossRef](#)] [[PubMed](#)]
52. Blöchl, P.E. Projector augmented-wave method. *Phys. Rev. B Condens. Matter Mater. Phys.* **1994**, *50*, 17953–17979. [[CrossRef](#)]
53. Kresse, G.; Joubert, D. From Ultrasoft Pseudopotentials to the Projector Augmented-Wave Method. *Phys. Rev. B Condens. Matter Mater. Phys.* **1999**, *59*, 1758. [[CrossRef](#)]
54. Ravishankar, S.; Bisquert, J.; Kirchartz, T. Interpretation of Mott–Schottky plots of photoanodes for water splitting. *Chem. Sci.* **2022**, *13*, 4828–4837. [[CrossRef](#)]

Disclaimer/Publisher’s Note: The statements, opinions and data contained in all publications are solely those of the individual author(s) and contributor(s) and not of MDPI and/or the editor(s). MDPI and/or the editor(s) disclaim responsibility for any injury to people or property resulting from any ideas, methods, instructions or products referred to in the content.